#### Section 1:

# Centrifugally Powered Pneumatic De-Icing for Helicopter Rotor Blades

NASA Award Number: NNX14AF54A

**Investigator(s):** Dr. Jose Palacios-The Pennsylvania State University, Dr. Joseph Szefi- Invercon, Doug Daley-Kaman Aerospace Corporation

# **Purpose**

The purpose of the current work is demonstrate the centrifugally powered de-icing technology on a full-scale helicopter rotor blade. Existent rotor blades were modified to accommodate the leading edge pneumatic de-icing concept. Full-scale hover testing was conducted under representative icing conditions at Kaman's whirl tower in Connecticut. The test demonstrated the capability of the innovative low-power, non-thermal centrifugally pumped de-icing system to debond thin layers of ice (<5 mm thick) on a full-span, full-chord hovering rotor, while using pressure differentials created by the rotating system.

# **Background**

Helicopter rotors are more susceptible to icing than the rest of the fuselage or fixed wing vehicles. The higher collection efficiency of rotor airfoils makes them accrete ice at a higher rate than thicker airfoils. Rotorcraft vehicles operate in atmospheric conditions where supercooled water particles are found.

Pneumatic de-icing systems tested in the past relied on pneumatic slip rings to transfer pressure to the rotor and to inflate the boots at the leading edge, increasing hub complexity. The boots also eroded during take-off and landing [1]. With advances in erosion resistant materials, and the application of patented rotor blade centrifugal pressure generation, the drawbacks of pneumatic de-icing for rotor blades could be addressed, providing a revolutionary low-power, non-thermal pneumatic de-icing system without the need for pneumatic slip rings.

## **Approach**

The centrifugally generated pressures produced in a 24 ft. radius KMAX blade rotating at 280 RPM were experimentally measured in previous work [2]. With these pressures in mind, two prototype de-icing systems were designed, fabricated and tested in Penn State's Adverse Environment Rotor Test Stand (AERTS) using a pneumatic slip-ring to provide system input pressures. The better performing prototype was fitted to an existing full-scale KMAX rotor blade. The modified blade was subsequently tested at Kaman's whirl tower under representative icing conditions using the centrifugally generated pressure differential as the system input pressure.

## **Accomplishments**

- Two centrifugally powered pneumatic de-icing systems designed and tested under representative icing conditions at Penn State AERTS
- A finite element method to predict the de-icing system's ability to delaminate accreted ice was validated
- One de-icing system design was chosen and installed on a full-scale KMAX blade
- Full-scale hover testing in severe icing conditions showcased the new technology's ability to operate using pressure differentials created by the rotating blades
- A portable icing cloud generator capable of reproducing FAR Part 25/29 Icing Envelope conditions was developed and fabricated to provide representative icing conditions for full scale tests

## **Prototype De-Icing System Designs**

Two centrifugally powered pneumatic de-icing systems were designed and fabricated. Prototype 1 consisted of a 0.03 in. thick 304 stainless steel leading edge cap held to blade surface via several flexible metallic ribs running along the blade span as seen in Figure 1. The ribs were constructed of 0.005 in. thick 1095 spring steel and bonded to the blade surface and inner cap surface with a high peel/high shear strength adhesive. These ribs and the adhesive are the primary load carrying structure of the system, and sizing was designed so that the system could withstand the centrifugal forces acting on the blade while still allowing the system to deform enough to promote ice delamination.

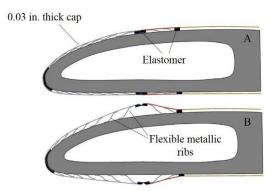


Figure 1. De-icing system prototype 1.

The second prototype de-icing system did not use the flexible metallic ribs. Instead, the pressurized region under the cap was continuous and the aft region of the cap was held to the blade surface using elastomer to seal the region as seen in Figure 2. Continuous spring steel ribs were wrapped

around the blade leading edge and bonded to the inner surface of the cap and outer surface of the blade to provide the load path for centrifugal forces in this design. These ribs were 4 in. (0.102 m) in width and 0.005 in. (0.127 mm.) thick and were bonded to the blade and inner cap surface in an alternating fashion along the blade span as illustrated in Figure 3.

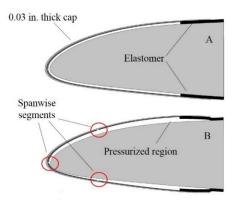
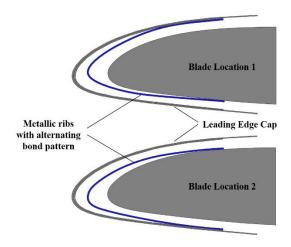


Figure 2. De-icing system prototype 2 in the un-deformed (A) and deformed (B) configuration.



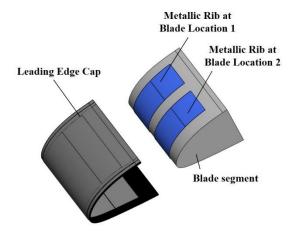


Figure 3. Exploded view schematic illustrating alternating bond pattern of inner metallic ribs used in prototype 2.

The cap was again constructed of 0.03 in. 304 stainless steel. However, spanwise segments were introduced at the leading edge and on the top and bottom airfoil surfaces. This was done to allow increase cap flexure in these areas, creating higher stresses to assist with ice delamination.

## **Initial De-Icing System Modeling**

Finite element modeling of both prototype designs was conducted using Abaqus finite element software to guide the system geometry selections. Transverse shear stresses along the outer surface of the leading edge cap were to be maximized so as to promote delamination of accreted ice. A 2-D model of the first prototype was used to determine the required size and spacing of the spring steel ribs used to hold the leading edge cap to the blade. The system was modeled as installed on a NACA 23012 airfoil with a chord of 16 in. (0.406 m.) and is depicted in Figure 4. Surface tie constraints were used to form the bond-lines between the spring steel slats and the blade and leading edge cap. To prevent element penetration between parts, surface-to-surface general contact was defined. Quadratic plane strain elements with reduced integration (CPE8R) were used. To match the span of the physical prototype, a plane strain thickness of 12 in. (0.4048 m.) was specified. A pressure of 4 psi (27579 Pa) was applied to the inner surface of the pressurized zones. For the initial design phases centrifugal forces were included in the model, however aerodynamic pressures were ignored.

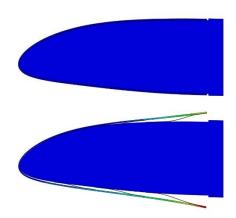


Figure 4. 2-D Abaqus finite element model of the first prototype deicing system in its undeformed (top) and deformed (bottom) state.

This process was repeated while spring steel slat dimensions and number were varied. A total of three slats were selected for the final design with widths of 1.5 in., 1.25 in., and 1 in. (38.1 mm., 30.9 mm., 25.4 mm.) from the trailing edge forward. Bond-lines were selected to be 0.25 in. (6.35 mm.) for each slat to allow for ease of manufacturing. The second prototype was modeled using the same techniques as the first using a 16 in. (0.406 m.) chord NACA 23012 blade. The leading edge cap was created as two separate 0.015 in. (0.381 mm.) thick stainless steel parts bonded together with surface tie constraints. Cap geometry and spanwise slats locations were representative of the

physical prototype. Surface tie constrains were used on all bond-lines between the elastomer and blade while surface to surface contact interactions to prevent solid body penetration. For simplicity, the continuous spring steel ribs used to hold the leading edge cap to the blade were assumed to not contribute significant stiffness to the system along the in-plane direction and were omitted from the finite element models.

Introduction of the elastomer into the design for the second prototype required the selection of a hyperelastic strain energy density model. Most rubber materials can be assumed to be isotropic and incompressible as described in [3] and therefore a Poisson's ratio of 0.5 was used. The Neo-Hookian strain energy density is derived from statistical mechanics and thermodynamic principles and is the simplest of the hyperelastic models, requiring only one coefficient determined from experimental test data. It is sufficiently accurate for strains of less than 40% [4]. For these reasons it was decided that the Neo-Hookian model would be used to model the elastomer. Abaqus accepts either strain energy material coefficients or material test data into its hyperelastic models. Uniaxial tension material test data for an EPDM elastomer with a shore hardness of 55A obtained in [5] is shown in Figure 5 and was used to define the model material.

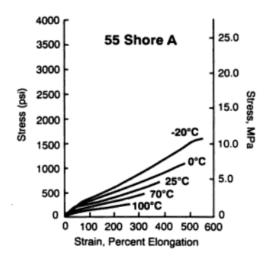


Figure 5. Uniaxial tension test data for EPDM from [5].

A free mesh technique was used on all parts in the assembly. 2-D plane strain reduced integration quadratic elements (CPE8R) were used for all parts. A sample result from the modeling of the second deicing system design is given in Figure 8.

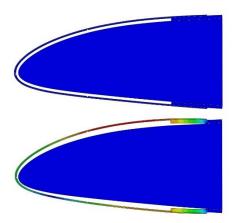


Figure 6. 2-D Abaqus finite element model of the second prototype in its undeformed (top) and deformed (bottom) state.

#### **Prototype Rotor Ice Testing**

Both prototype deicing systems were installed on 12 in. (0.3048 m.) truncated paddle sections of a Kaman KMAX blade and mounted at the tip of a 36 in. (0.914 m.) radius carrier blade. A schematic of the configuration at the AERTS facility is shown in Figure 7.

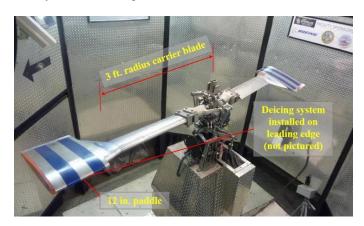


Figure 7. AERTS facility used for prototype ice testing.

To evaluate the systems deicing capability, a test matrix was developed which reproduced the centrifugally generated pressure differential experienced along a 24 ft. (7.3 m.) radius blade operating at 280 RPM. These pressures were experimentally measured in previous work and are shown in Figure 8. Since the span truncated prototype blades are not capable of producing the necessary pressures, a pneumatic slip ring was used to deliver the desired pressures to the deicing system.

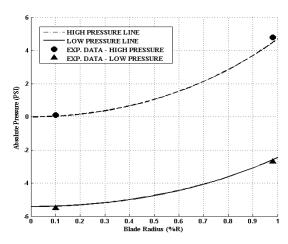


Figure 8. Pressure differential available for centrifugal pumping measured along span of a 24 ft. (7.3 m.) radius rotor blade.

Icing conditions for prototype ice tests were as follows: LWC=1.9 g/m³, MVD=20 $\mu$ m, T=-14°C. Due to facility limitations and blade structural concerns, rotor speeds were limited to those which reproduced centrifugal forces seen along the inboard half of a full-scale KMAX blade. Note that because the available pressure differential along the full-scale blade span is constant, this prototype configuration allowed for testing of the representative inboard region of a full-scale system. A sample photograph of the second prototype de-icing system is provided in

Figure 9.

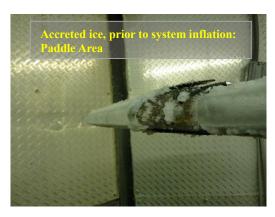




Figure 9. First prototype before and after system deployment.

A comparison of the performance of both prototype deicing systems is provided in

Figure 10. The ice thickness required for delamination was normalized with respect to g's of centrifugal acceleration because prototype 1 and 2 were tested at different rotor speeds. Results showed that an increase in system input pressure leads to a decrease in ice thickness that can be delaminated. There was a 58% decrease in required ice thickness from prototype 1 to prototype 2, therefore this design was chosen for full-scale blade integration.

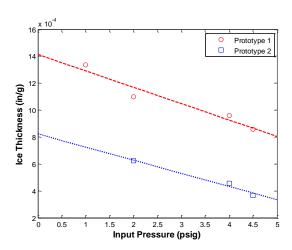


Figure 10. Comparison of prototype performances with varying system input pressure.

# Validation of Cohesive Zone Methods for De-icing System Performance Predictions

The ice-leading edge interface of the de-icing system can be modeled using the cohesive zone method, a technique applied in predicting composite delamination crack growth [6]. This method is governed by traction-separation laws which assume a decrease in the load carrying capability of the interfacial cohesive layer as the two adhered substrates are separated. Once the adherends reach a critical separation distance as defined by material cohesive and damage properties, that region can no longer carry any load and is said to be failed [7]. A sample traction-separation curve for single mode loading is provided in Figure 11.

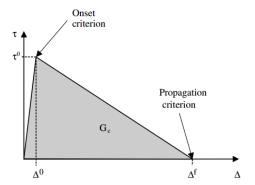


Figure 11. Sample traction separation curve for single mode loading [7].

Using cohesive properties of the substrates, which were experimentally measured in NASA LEARN Phase I, the critical mixed-mode separation,  $\Delta f$  in Figure 11, can be calculated. For the current application this separation is 2.7e<sup>-4</sup> in (6.88µm).

Abaqus finite element software is capable of predicting the Mode I and Mode II/III separations by defining a cohesive surface at the interface of the ice and metallic leading edge cap. Representative ice shapes were produced using Lewice. 2-D parts were created from these ice shapes and were used in the delamination prediction study. An example of the created ice shape parts is provided in Figure 12.

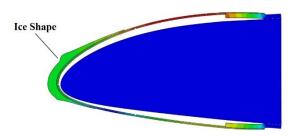


Figure 12. Representative ice shape created using Lewice for de-icing system delamination predictions in Abaqus.

By varying the input pressure to the pneumatic de-icing system, a relationship between the percentage of ice delaminated and pressure can be obtained for each ice shape. Figure 13 illustrates an example output from one Abaqus delamination simulation at a single pressure. The horizontal line represents the critical mixed-mode nodal separation, and total separation is the magnitude of the Mode I and Mode II/III separations. In Figure 13, for any portion of the total separation curve that lies above the critical failure separation value, this portion of the ice shape has delaminated.

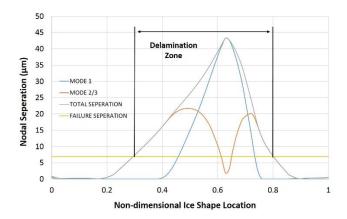


Figure 13. Sample Abaqus delamination study output. Horizontal axis represents the non-dimensional arc-length position along the ice shape.

With knowledge of the percent ice shape bond-line that has not failed following de-icing system actuation and the adhesion strength of ice to stainless steel, the centrifugal forces required to shed the ice shape can be calculated and compared to the centrifugal forces actually acting on the ice. If the centrifugal forces acting on the ice are greater than those required, the ice is shed. Ice thickness along the non-dimensional blade radius before and after a successful shedding event is given in Figure 14. For this case, the deicing system was installed on the outer 20% of the blade to mimic the configuration tested in the AERTS facility.

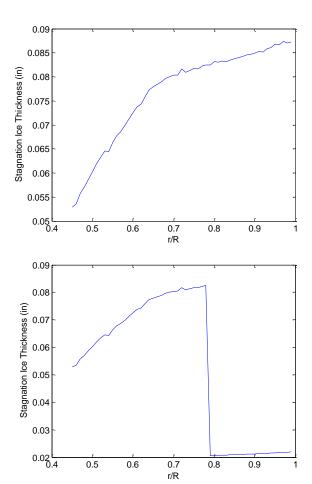


Figure 14. Example of ice shedding calculation before (top) and after (bottom) pneumatic de-icing system actuation. Note that the de-icing system tested in AERTS was installed from r/R=0.8-R.

To validate the described process, ice shapes with thicknesses similar to those encountered during prototype testing at the AERTS facility were created as Abaqus parts. In the Abaqus model, de-icing system pressure was varied until a large enough portion of the bond-line had failed to allow centrifugal forces to shed the ice shape. Typically, required values of percent bond-line failure were about 45% of the total bond-line length. An example result of this parametric study is provided in Figure 15. Note the discontinuity in percent ice shape delaminated in Figure 15, where the cohesive zone undergoes a rapid separation. It is in this region that a sufficient enough percent of the bond-line fails to allow centrifugal forces to shed the ice shape.

However, due to the rapid delamination in this region, the amount of ice that remains bonded is not exactly known and therefore must be estimated, leading to an uncertainty in the prediction.

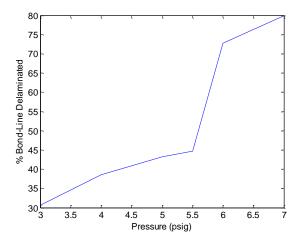


Figure 15. Sample result of percent ice shape bond-line delaminated prediction from Abaqus.

The described prediction process was repeated for each icing condition tested in the AERTS facility on prototype 2. A comparison of the Abaqus model predictions to experimental test results is presented in Figure 16. Model predictions consistently over predict the ice thickness required for successful shedding, however these over predictions are small (about 10%) and allow for a conservative estimation of the de-icing system's performance capabilities. These results provide confidence in the described method's ability to be used as a design tool to study the effects of changes to future de-icing system configurations.

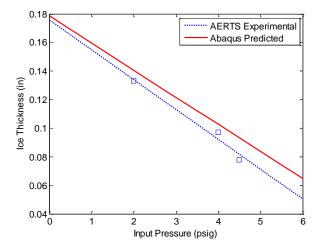


Figure 16. Comparison of experimentally measured ice thickness required for shedding after pneumatic de-icing system actuation to Abaqus predicted values.

#### **Full-Scale Blade Modifications**

A 24 ft. (7.3 m.) radius Kaman KMAX blade was supplied by Kaman and delivered to Penn State for installation of the deicing system. Lead by Invercon, the blade was fitted with a pneumatic deicing system similar to the second prototype evaluated at Penn State AERTS. The deicing system protected an 8 ft. (2.4 m.) section of the blade measuring from the tip inboard as depicted in Figure 17. Modifications were performed at Penn State and blade balancing was conducted by Kaman at their Bloomfield, CT location.



Figure 17. Modified KMAX blade on Kaman whirl tower.

Prototype ice testing proved the second prototype's ability to delaminate accreted ice using a pneumatic slip-ring to provide air pressure to the de-icing system. Full-scale hover testing was conducted at Kaman's whirl tower in Connecticut to show the system's ability to operate using only centrifugally generated pressures.

The leading edge cap was constructed of two 0.0015 in. (0.381 mm.) thick 304 stainless steel sheets bonded together and pressed with a die into the shape of a NACA 23012 airfoil. As with the prototype, the inner cap was segmented spanwise along the leading edge and 1 in. (25.4 mm.) aft on both upper and lower surfaces. The outer 0.01 in. (0.254 mm.) protection layer did not have any discontinuities, providing a smooth aerodynamic surface. Thirteen 6 in. (152.4 mm.) by 4 in. (101.6 mm.) by 0.005 in. (0.127 mm.) thick 1095 spring steel sheets were bonded in an alternating fashion to the top and bottom surface of the blade in the spanwise direction as depicted in Figure 18 and Figure 19. This was done to increase the surface area bonded to the blade while not impeding the cap motion during system actuation. EPDM elastomer was bonded to the blade and inner cap surface to form a flexible seal on all edges. In addition, energy is stored in the spring sheets when elastically deformed to follow the blade contour during installation. This stored energy assists the deicing system in moving the leading edge cap during inflation.

A total bond area of 282 in<sup>2</sup> (1819 cm<sup>2</sup>) between the elastomer and spring steel provided a factor of safety of 13, ensuring the deicing system would withstand centrifugal forces during rotation. Strips of 0.015 in. (0.381 mm.) thick

304 stainless steel were bonded on top of the elastomer to reduce the likelihood of tearing as shown in Figure 18 and Figure 19.

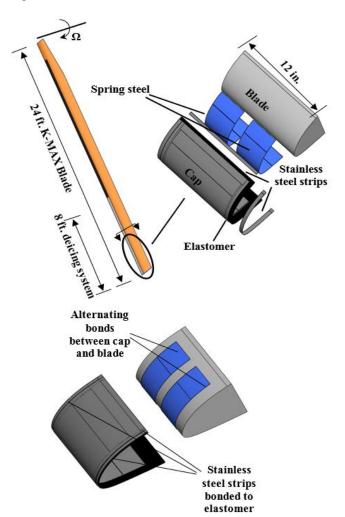


Figure 18. Schematic of de-icing system assembly installed on full-scale blade.

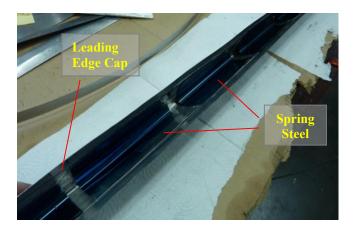


Figure 19. Schematic of alternating spring steel sheets bonded to inner surface of leading edge cap.

During bench-top testing, pressure was supplied to the system via a 0.165 in. (4.191 mm.) diameter tube running

along the blade leading edge and entered the system at the inboard cap edge. A 0.75 in. (19.05 mm.) diameter low pressure line was installed in the center of the blade and ran from root to tip. This line provides low pressure during rotation. A 24V microvalve located at the blade root was cycled at 0.07 Hz to open and close the 0.165 in. diameter line to atmospheric pressure. When open to atmosphere, centrifugal loads pressurize the air inside the line thus inflating the deicing system. 10 mW of power and a 5V signal to the valve was supplied through a slip-ring and controlled by a data acquisition computer. A Hall sensor was installed near the inboard edge of the system as a method of monitoring the motion of the cap.

The final full-scale pneumatic deicing system provides significant weight and power savings compared to electrothermal deicing systems, which typically require 25 W/in² for effective ice protection³. The only electrical power draw of the pneumatic system is 10 mW to power a microvalve. Also, a power loss is introduced to the main rotor while compressing the air used to inflate the system, however this loss is negligible (~1 W).

The high power requirements of electrothermal systems often require the addition of additional alternators resulting in a final system weight of 100-200 lbs. (45.4 kg. to 90.7 kg.). Since the pneumatic system consists of only the modification to the leading edge cap and lightweight hoses, and does not require heavy non-rotating electrical components, its weight is comparable to that of the existing protective leading edge cap.

#### **Full-Scale Icing Testing**

Testing of the centrifugally powered pneumatic deicing system was conducted at Kaman's whirl stand located in Bloomfield, CT. during the month of February (February 9 – 13 2015). The portable icing cloud generator was also tested during this time, however due to power limitations, sufficient compressed air was not available thus reducing the number of nozzles that could be operated from twelve to four. For this reason the ability of the cloud generator to operate in a cold environment and produce a realistic icing cloud with measurable ice accretion was demonstrated separately before testing the deicing system. In addition to using the portable spray system during initial testing, two water pressure lines producing 2400 psi (16.55 MPa) each and equipped with a 45<sup>o</sup> angle non-air assisted aerosolizing spray nozzle at their tips were used to increase the liquid water concentration in the cloud, speeding-up the ice accretion process. The benefit of direct water pressure nozzles is that the large air flow rates needed for the NASA nozzles in the portable icing system is not required. For the purpose of this test, providing uncontrolled water droplet mixtures of super-large droplets (estimated to range between 40 µm to 400 µm) provides a conservative worst-case ice accretion scenario, since larger droplets at high liquid water concentrations will be generated. The larger particles size and water content will increase the ice accretion impingement limits. Large droplets were visually observed at the exit of the nozzle, and a reduction on droplet size was qualitatively observed at approximately 20 ft. (6.09 m.) from the water output. The water pressure lines were mounted on the ground providing sufficient distance for the reduction in size of the water droplets created. The cloud dissipation provided a more realistic (but unmeasured) droplet size to enter the rotor plane. The cloud LWC was calculated to be 0.6 g/cm³ with an assumed MVD range of 40-200µm at the rotor plane. A photograph of the final setup is shown in Figure 20. Tests were conducted at static air temperatures ranging from -5°C to -15°C, thus spanning a large portion of the Appendix C icing envelope outlined in [8].

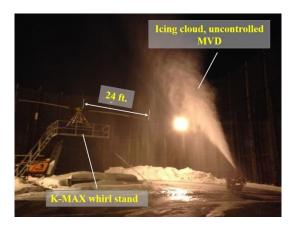


Figure 20. Final icing cloud set up for de-icing system testing.

Two different test methodologies for ice protection were explored with the pneumatic deicing system: continuous ice protection and single deicing occurrence. For the continuous ice protection method, ice was allowed to accrete for a set amount of time with the deicing system turned off. At set time intervals the deicing system was turned on and cycled three times at 0.07 Hz and subsequently turned off. This process was repeated throughout the entire test multiple times in an attempt to exercise the ability of the system to operate as it is envisioned during flight (intermittent operation post ice accretion for controlled time intervals). The single deicing method tests consisted of accreting ice for a set time length with the deicing system turned off followed by a 30 second period of cycling the system once the predetermined icing time had elapsed. After the deicing system was turned off, the rotor was also spun down. A schematic of the test process for single-shot deicing is provided in Figure 21.

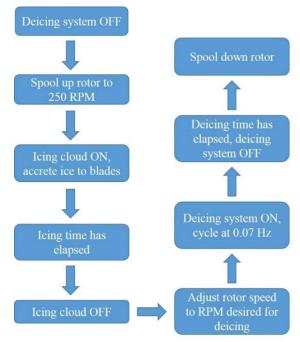


Figure 21. Method for single-shot de-icing testing.

For both deicing methods, system deployment was monitored using real-time time data provided by a Hall sensor. A sample of this output is displayed in Figure 22. In the Hall sensor output, system inflation and deflation corresponds to motion of the of airfoil surface. An increase in voltage represents system inflation, while deflation causes a decrease in voltage. Selected icing times were determined by measuring accreted ice thicknesses in early tests. Rotor speed for ice accretion was 250 RPM and was increased to 270 RPM for deicing system deployment in the single shot deicing tests. Rotor speed was held constant at 270 RPM for the continuous ice protection tests. Several tests were also conducted at a deicing rotor speed of 230 RPM to observe the deicing systems ability to operate at lower input pressures and centrifugal forces acting on the ice. Both test methods were successful to remove accreted ice and proved the ability to protect full-scale rotor blades with semi-passive centrifugally powered pneumatic deicing systems. Selected successful deicing test results are presented in Table 1. Detached ice thicknesses measured as small as 0.08 in. (2.032 mm.), and were successfully shed during the single shot deicing tests for a rotor speed of 270 RPM and at temperatures as low as -15°C. Ice thicknesses for a rotor speed of 230 RPM were measured to be as small as 0.1 in. (2.54 mm.). It is worth noting that the minimum thickness required for electro thermal deicing systems is 0.3 in (7.62) mm) <sup>3</sup>. A sample photograph of the protected result of semicontinuous ice protection are shown in Figure 23.

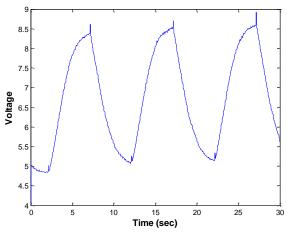


Figure 22. Hall sensor output voltage from a standard de-icing test.

Table 1. Sample de-icing test results.

Temp.	Ice RPM	De-ice RPM	Ice Thick.
(°C)			(in)
-10	250	230	0.1
-12	250	230	0.15
-14	250	270	0.08

The large droplets produced by the non-air assisted nozzles created ice shapes much more severe than what would be encountered in flight. Impingement limits were noted to be further aft than those of standard icing conditions, creating a more difficult ice protection scenario for the deicing system. An example of the severe ice shapes encountered during testing is illustrated in

Figure 24. These severe ice shapes were successfully removed by the proposed pneumatic deicing system.

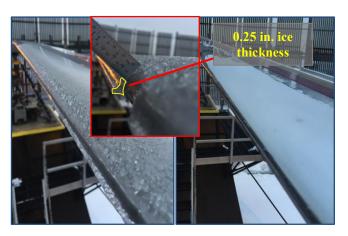


Figure 23. Comparison of protected (right) and unprotected (left) blades after de-icing test.

During icing tests, it was noticed that a small section of the protected blade consistently left residual ice after the deicing system had been inflated as seen in Figure 25. It was determined that this portion of the cap was unable to deform completely and thus unable to create the stresses necessary for ice delamination. The restriction of cap movement in this area was attributed to unwanted adhesive bonding during system manufacturing.



Figure 24. Large water droplets during ice testing created ice shapes more severe than typically encountered.



Figure 25. A small portion of the leading edge cap consistently left accreted ice behind after inflation. This was attributed to unwanted adhesive bonding during manufacturing,

#### **CONCLUSIONS**

Two prototype centrifugally powered pneumatic deicing systems were developed, fabricated and tested. The system is formed by a stainless steel leading edge sealed to the blade. The metal is deformed by pressures generated by centrifugal forces acting on a column of air inside the blade. Input pressures to the system during truncated span rotor blade prototype testing were provided via a pneumatic slip ring. Results from prototype ice testing showed that a configuration concentrating stresses within the ice accretion impingement limits delaminated ice shapes 69% thinner than deicing configurations that had maximum stresses on a further aft location. A system introducing maximum stresses within the ice impingement limits and consisting of a single pressurized zone was installed on the outboard 8 ft. (2.4 m.) section of a 24 ft. (7.3 m.) radius KMAX blade. Removal of the existing stainless steel KMAX leading edge cap allowed the deicing system to be installed in its place (0.03 in thick, 0.762 mm), thus maintaining the original aerodynamic shape of the blade. Full-scale qualitative icing tests were conducted at Kaman's whirl stand. Unlike prototype testing using truncated blades, input pressures to the system were produced by centrifugal forces. The deicing system was successfully tested at static air temperatures within the FAR Part 25/29 Standard Icing Envelope and was able to delaminate ice thicknesses as small as 0.08 in. (7.62 mm.) Specific conclusions that can be drawn from the conducted research are:

- 1) The current centrifugally powered pneumatic deicing system is capable of delaminating ice thicknesses as small as 0.08 in. (2.032 mm.) at temperatures of -15°C along a blade section spanning 0.6r to the tip of a 24 ft. (7.3 m.) blade. This ice thickness is 73% less than ice thickness required by electro thermal deicing systems (0.3 in., 7.62 mm.).
- 2) The developed pneumatic deicing system presents significant power and weight savings compared to electrothermal deicing systems. A microvalve requiring 10mW and a small power loss due to air compression (~1W) are the only power sources required for the pneumatic deicing system. The pneumatic system directly replaces existent leading edge caps and introduces minimal weight related to plastic pressure lines spanning the length of the rotor. The system does not require heavy nonrotating electrical components, and its weight is negligibly more than that of the existing protective leading edge cap.
- 3) A portable icing cloud generator was designed, fabricated and tested. The system was able to provide controllable water droplet size. The system requires a 30 HP air compressor to power all twelve nozzles needed to provide representative in-flight liquid water concentrations.

**Current TRL:** Number. See NASA Systems Engineering Handbook (NASA/SP-2007-6105) for more information on Technology Readiness Level (TRL).

# **Publications and Patent Applications**

 Presented at the 71<sup>st</sup> AHS Forum in Virginia Beach, VA

# Section 2: Centrifugally Powered Swashplateless Actuator

NASA Award Number: NNX14AF54A

Investigator(s): Dr. Joseph Szefi – Invercon LLC

#### Introduction

For several decades, the rotorcraft community has recognized the potential performance benefits that could be gained by incorporating active surfaces on rotor blades, particularly trailing edge flaps [9]. Over the years, several researchers have detailed the vibration control benefits provided by flaps, while several also have envisioned rotors that rely on trailing edge flaps to provide primary control, thus completely eliminating the need for a mechanical swashplate assembly. Analytical investigations in the literature suggest that flap displacements of  $\pm 15^{\circ}$  to  $\pm 20^{\circ}$  are required to achieve swashplateless forward flight [10]-[14]. It must be noted that Kaman's K-MAX helicopter already achieves primary control through the motion of servoflaps, although a mechanical linkage from the servoflap to the hub is still required to achieve the required servoflap motion.

Moreover, several researchers have attempted to realize flap motion through the use of on-blade actuators, mostly in the form piezoelectric-based and electromechanical devices. Both of these solutions, however, introduce a number of new blade and aircraft design issues. In the case of piezoelectric devices, the active PZT material is lead-based and has a similar density to steel. In addition, piezoelectric devices require an ancillary motion amplification system which also adds unwanted blade weight. Because of this added weight, blades must be reinforced in the area of installation to accommodate the increased centrifugal forces (CF) introduced by the system. On top of weight concerns, high voltage must be routed to the device through advanced electrical slip rings, and electrical amplifiers must be onboard to generate the actuator signals, adding more weight. Thus far, piezoelectric devices have also exhibited limited stroke in the range of  $\pm$  3°. More traditional, and often very complex, electromechanical design solutions also have similar unwanted added weight and slip ring issues and usually suffer from mechanical wear issues introduced by increased internal mechanism friction caused by extreme CF loading.

In the current work, Invercon has proposed a radical departure from these design concepts, one which in which the actuator output is powered using an on-blade, centrifugally developed pressure differential, introducing extremely little blade weight. In Figure 26, a schematic illustrates this concept. It would be advantageous to utilize the large centripetal acceleration created by the rotor to generate an on-blade air pressure differential for actuation, thus eliminating both the need to transmit high amounts of

electrical power to the rotating frame and the need for heavy, traditional actuators that can negatively impact overall rotor blade weight. A conceptual schematic of a centrifugally powered pneumatic actuator that powers a trailing edge flap is pictured in Figure 27. Invercon's actuation concept is directly aligned with the objectives of NASA's Subsonic Rotary Wing Project, having the potential to enable more efficient flight, enhance vehicle maneuverability, allow for multi-mission vehicle configurations, reduce exterior noise, and generally enhance the competiveness of US rotary winged vehicles in the civil sector.

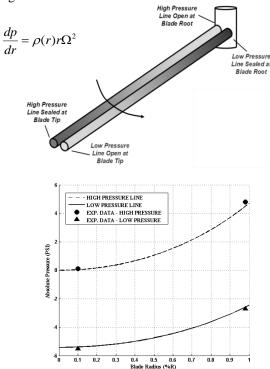


Figure 26. a) Schematic of Invercon's centrifugally generated pressure differential concept for actuation, and b) predicted pressure and experimentally measured pressure values (280 RPM, 24 ft. radius rotor)

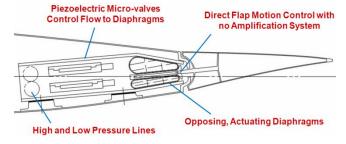


Figure 27. Conceptual centrifugally powered pneumatic actuator powering a trailing edge flap

## **Objectives**

Under Penn State's Phase II LEARN program, entitled "Centrifugally Powered Pneumatic De-Icing for Helicopter Rotor Blades", Invercon was a subcontractor and fabricated and installed the pneumatic de-icing actuation system on the KMAX blades. Incidentally, the blades that were used for the Phase II de-icing test were the same blades that were utilized for Invercon's NASA LEARN Phase I pneumatic

actuator test. Therefore, significant NASA funding was already allocated to modify these blades for trailing edge pneumatic actuator testing. Invercon's goal in the current study was to concurrently test a next generation pneumatic flap actuator along with the pneumatic de-icing actuator. The objective of this additional test was to validate that next generation, high flow, pneumatic valves are fully-functional under full-scale CF. Ultimately, Invercon went further and fabricated and tested a full-scale swashplateless actuator sized for a UH-60 rotor. The actuator incorporates novel, high flow pneumatic valves that were validated under full-scale CF.

# **Approach**

Prior to beginning this research effort, Invercon had already demonstrated a new, high flow valve design concept on the bench that incorporated Parker Hannifin's VIVA piezoelectric actuators, pictured in Figure 28. To ensure this design concept could operate under representative rotor CF, Invercon first tested it in a centrifuge test stand. Subsequently, Invercon designed and fabricated a next generation actuator capable of achieving ± 15° deflection and also fit within the geometry constraints of the modified blade cavity. The actuator was then bench tested, installed in the modified KMAX blade, and shipped to Kaman for spin testing. During testing, small particles within the inboard pneumatic volume were shed under high CF and tended to clog and bind the valve system, rendering the actuator spin tests unsuccessful. With new lessons learned, Invercon then designed and fabricated a full-scale, next generation actuator that was capable of operating despite FOD in the system. Bench tests of this actuator clearly demonstrate the feasibility of lightweight, high torque, high displacement flap actuation for swashplateless rotors.

# **Accomplishments**

- Design, fabricated and CF tested a novel new high flow butterfly valve
- Incorporated butterfly valve into scaled, compact, swashplateless actuator for full-scale spin testing
- Based on lessons learned during spin testing, reimagined valve approach and pursued "piloted" valve design
- Designed and fabricated full-scale, next generation pneumatic actuator with piloted valve approach
- Using representative air flows and pressures, experimentally demonstrated ability to provide sufficient torque and displacement for swashplateless actuation in UH-60 sized rotor.

# **High Flow Valve Design and Testing**

The basic high flow valve design concept incorporated in the new actuator design is pictured in Figure 28. Unlike previous valve concepts, the incoming air follows a relatively straight path through an inline butterfly valves with a large diameter that would be placed at both the inboard and outboard ends of the diaphragms. The valve discs are actuated using a piezoelectric VIVA actuator produced by Parker Hannifin, which are capable of delivering up to 1/8" of displacement and 7 lbs. of force at frequencies up to 300 Hz and weigh only 14 g. Under a separate research effort, Invercon has experimentally demonstrated this mechanism's ability to successfully function under CF loading levels of up to 750 g's. Here, valve manifolds are not required which greatly reduces complexity and overall weight. Also, because the butterfly valves allow for orders of magnitude higher flow as compared to previous test actuator valves, the actuator should be capable of delivering the higher torque and displacement at higher frequencies.

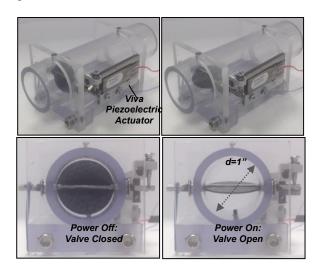


Figure 28. High flow butterfly valve system developed at Invercon

After determining that the butterfly valve design was a viable flow control solution, Invercon then modified the design so that a set of stacked inboard and outboard valves could fit within the cavity of the modified KMAX blade, as pictured in Figure 29. The resulting valve mechanism was a set of flat, rectangular butterfly valves that only needed to rotate roughly 20° to fully open or close. For both the inboard and outboard set of valves, the Parker Hannifin piezo actuators again provided the necessary force and displacement to activate the valves. The valve operation is illustrated in Figure 30 where the set of inboard valves is depicted for both when the top diaphragm is open to the high pressure and when the bottom diaphragm is open the high pressure.

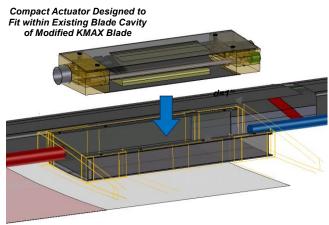
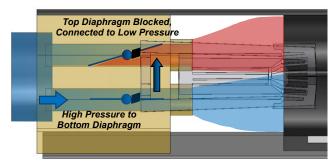


Figure 29. Scaled, compact actuator designed to fit within existing modified blade cavity.

#### Inboard Side of Actuator



#### Inboard Side of Actuator

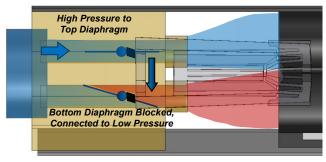


Figure 30. High flow butterfly valve system incorporated into compact actuator

Subsequent to testing this valve design on the bench to confirm it can control flow under representative pressures, Invercon then tested its operation in a centrifuge test stand, as pictured Figure 31, under representative CF loading. Using a hall sensor to measure valve displacement, Invercon confirmed that the valve setup could operate under 500 g's, which is the amount of CF the valves would be subject to on the KMAX blade. Upon confirming the proper motion of the butterfly flaps under CF, Invercon then completed the overall actuator design, which was similar to the Phase I actuator and

included a set of flexible top and bottom diaphragms, a center divider to output displacement, a torque shaft to apply variable output resistance, and a rotary motion sensor. The actuator fabrication was then completed and initial bench testing was conducted to confirm actuator performance given a representative flow and pressure source. Cross-sectional views of the actuator's extreme displacements of  $\pm 15^{\circ}$  are depicted in Figure 32. Additionally, a picture of the actuator installed in the modified KMAX blade cavity is shown in Figure 33.

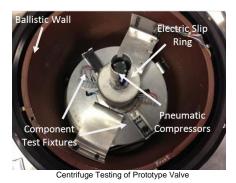


Figure 31. Centrifuge testing of valve under 500 g's of CF loading.

High Pressure in Top Diaphragm High Pressure in Bottom Diaphragm

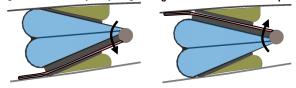


Figure 32. Actuator diaphragm cross-section for both ±15° displacement.



Figure 33. Compact actuator installed in KMAX blade prior to spin testing.

After successfully conducting the pneumatic de-icing portion of the spin testing, Invercon and PSU then attempted to experimentally validate the pneumatic actuator's performance using centrifugal pumping. Upon activating the valves, however, very little actuator output displacement was observed. Invercon and PSU then spent the remaining portion of the allotted test time trying to determine the reason for the lack of motion. Ultimately, the actuator was removed and inspected on the bench, and it was revealed that loose,

honeycomb FOD from the inboard supply line had collected in the inboard set of valves under the high CF, as pictured in Figure 34. Prior to spin testing, the inboard supply line was bored out to ensure a uniform 0.75" diameter along the entire length of the inboard blade section. During this operation, the drill bit necessarily created some loose honeycomb particles. Despite every effort to clean and vacuum this loose debris prior to testing, it was apparent that the high CF released those small particles that the vacuum could not. Ultimately, the FOD had compromised the actuator's operation to such a degree that useful results could not be obtained. Although a disappointing test result, Invercon then set about to re-imagine the actuator's design and proceeded to design, fabricate, and test a new actuator design to avoid this problem while also allowing for higher air flow and relying on CF tested piezo valves. The design and testing of this next generation actuator is detailed in the next section.

Loose FOD from Blade Interior Collected in Inboard Valves During Spin Testing

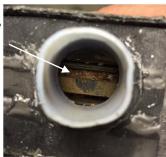


Figure 34. Loose honeycomb FOD released under CF, thus clogging inboard butterfly valves.

# Pneumatic Actuator Design with High Flow, Piloted Valves

As was evident after Phase I testing of the first generation pneumatic actuator, valve technology must be improved to enable higher flow rates to improve actuator performance at higher frequencies in general. Invercon attempted to address this issue with the butterfly valve design concept as detailed above. The spin test, however, revealed a shortcoming of this approach in that it was readily clogged, and perhaps a better approach would rely on less moving valve parts that could potentially be compromised.

Another valve design approach to achieve higher flow is through the use of piloted valve technology. In Figure 35, a schematic of a high flow, piloted piezoelectric valve is shown. Instead of the piezoelectric bender controlling flow into and out of the diaphragm, it instead controls flow into a small volume within the valve that causes a piston to move, which then in turn opens high flow orifices to either the high or low pressure sources.

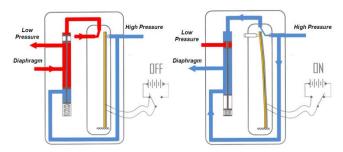
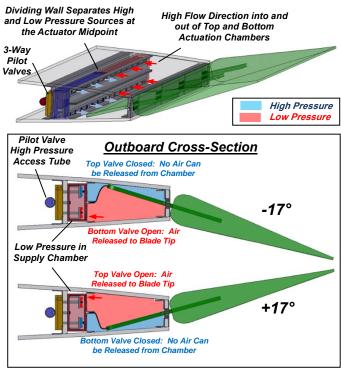


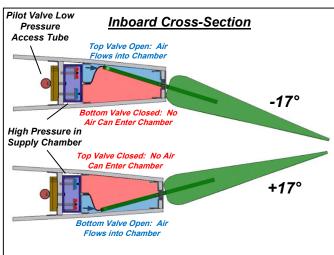
Figure 35. Basic example of piloted valve technology for flow amplification.

However, a piston-based, piloted valve like that shown in Figure 35 would typically not operate properly in the extremely high centripetal acceleration it would experience on a rotor blade. Therefore, a specialized piloted valve design would need to be developed that could deliver high flow to the pneumatic actuator diaphragms under extreme CF.

Following the unsuccessful spin test of the butterfly valve approach, Invercon then focused on developing a new high flow valve design that is based on a piloted approach. Invercon's goal was to design, fabricate, and bench test a full-scale pneumatic actuator that demonstrates the feasibility of swashplateless actuation while relying on valve technology that has been previously validated in high CF environments in multiple spin tests.

Invercon has successfully developed a high flow pneumatic actuator that relies upon piloted valve technology. In addition, the piezoelectric pilot valves that are employed are identical to those used in the Phase I spin test and thus are experimentally proven to operate in high CF environments. In Figure 36-Figure 38, multiple schematics demonstrate how this new actuator design functions. The actuator depicted in the figures was designed to fit within the profile of a UH-60 sized rotor. The main high and low pressure lines consist of rectangular, composite tubing that allows for high flow to and from the actuator. The three-way pilot valves mounted on the forward side of the pressure supply tubing have access to both the high and low pressure sources through special access tubing, shown in the lower illustration in Figure 36. The outputs of the pilot valves are connected to the four pilot diaphragms which can either seal or unseal the supply volumes in relation to the actuating chambers. In other words, the pilot diaphragms either inflate or deflate to allow for high flow into or out of the actuating chambers through slots machined into the tubing walls. Depending on the controller command signal for the flap displacement, the pilot valves tune the pressures in the pilot diaphragms to then adjust the pressure in the actuating chambers. The high flow into and out of the actuating chambers then occurs through the slots spanning entire span of the actuator. The result is high bandwidth, high torque actuation allowing for swashplateless flap actuation, all while adding extremely little blade weight (~2.5 lbs for flap/actuator system) and using insignificant electrical power (< 1 Watt).





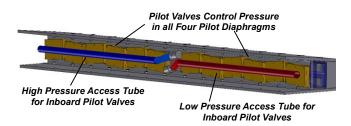


Figure 36. Graphical overview of piloted valve operation for next generation pneumatic flap actuator.

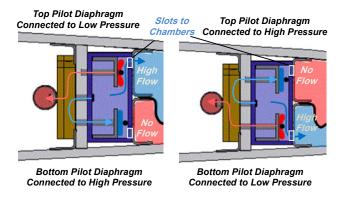


Figure 37. Close up view of pilot diaphragms and flow control into and out of actuating chambers.

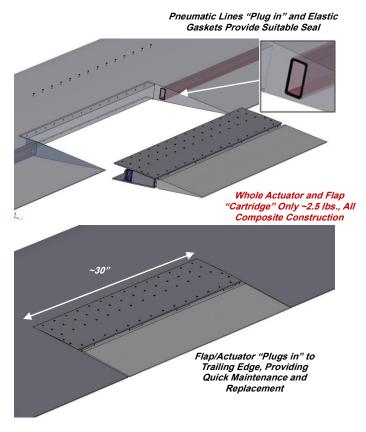


Figure 38. Schematic illustrating ease of flap/actuator system installation, maintenance, and replacement.

The actuating chambers are confined by the top and bottom actuator skins, and are separated by a rigid dividing flap. A flexible, neoprene membrane connects from the end of the dividing flap to the thickness midpoint of aft side of the supply tubes and side walls. The dividing flap is hinged along its entire length by two 1/4" x 1/4" neoprene layer strips that are sandwiched and bonded to either side of the flap and the actuator housing. In this manner, the flap has flexibility to move through its entire range of motion  $(-17^{\circ} \text{ to } +17^{\circ})$  with little resistance while maintaining a complete seal between the upper and lower actuating chambers. As a result, the actuator's output torque is maximized through its entire stroke, including the point of maximum displacement. This performance characteristic is an important distinction between this type of actuation and that of a piezoelectric actuator, for instance, which has zero torque output at its maximum deflection. The entire actuator housing can be fabricated using lightweight, composite materials resulting in an extremely light and flexible flap/actuator system. Additionally, as shown in Figure 38, the entire flap/actuator system can be readily "plugged" into the trailing edge, allowing for simple actuator replacement in the field.

#### **Next Generation Pneumatic Actuator Fabrication**

Following the completion of the detailed actuator design illustrated in Figure 36-Figure 38, Invercon then fabricated a full-scale pneumatic actuator that is sized to "plug" into the trailing edge of a UH-60 blade and fit entirely within the proscribed blade profile. The entire actuator consists of lightweight composites, flexible neoprene membranes, and of CF-tested, miniature piezo valves. Consequently, the actuator can tolerate typically blade flexing as would be experienced in operation. In

Figure 39 -

Figure 43, the actuator construction is depicted. In Figure 44, the flap/actuator system is pictured plugging into a mock UH-60 trailing edge. A thorough range of experimental testing was conducted to demonstrate the acutator's potential and is summarized in the next section.



Figure 39. Actuator prior to affixing upper and lower skins

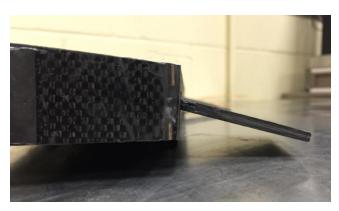


Figure 40. Side view demonstrating considerable actuator stroke (± 17°)

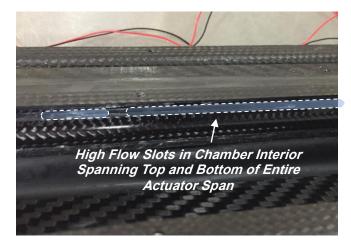


Figure 41. High flow slots provide extremely high flow rates into and out of actuating volumes

# Pilot Tubes Ensure 3-Way Valves have Access to both High and Low Pressures

Figure 42. View illustrating how pilot valves have access to both high and low pressure sources

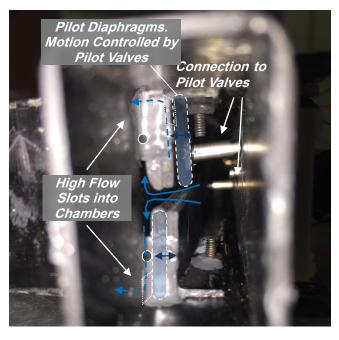


Figure 43. View of interior of main pneumatic supply volumes with pilot diaphragms

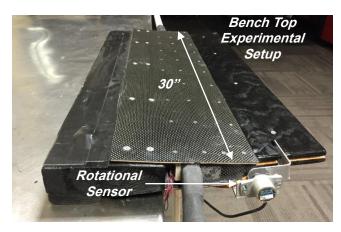


Figure 44. Actuator/flap system installed on mock UH-60 trailing edge

# **Experimental Testing of Next Generation Pneumatic Actuator**

#### Laboratory Pressure and Flow Source

In order to replicate the pressure and flow that would be available on a UH-60 sized rotor, a regenerative blower capable of delivering a flow of up to 4,300 in^3/s at a maximum pressure of 5 psi was employed, as shown in Figure 45. A blower of this type is needed because typical laboratory compressors cannot supply nearly enough flow as would be provided by a rotor blade. In combination with the blower, piping with an internal diameter of 3/4" is used before and after the actuator location to simulate the length of pipe in a rotor blade. Therefore, the overall system length can be made to equal that of a UH-60 blade, with a maximum pressure differential of 5 psi between the inlet and exit locations, which would be the case for centrifugal air pumping on a UH-60 blade.

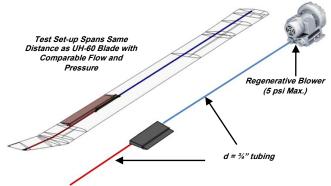


Figure 45. Regenerative blower set-up to provide mimic flow and pressure to available on a UH-60 blade.

#### Flap Stiffness

In order to apply a torsional stiffness to the flap output, a test fixture was built such that when the flap deflected it also deformed a series of cantilevered, spring steel beams rigidly anchored near the flap hinge point. Each beam was 1" wide and 0.063" thick and contacted the flap at a length of 2.5". An in-line force gauge was used to determine that with 400 in-lb of applied torque, the flap and beam deflected 15°. By added multiple beams, several different flap stiffnesses could be simulated and thus an overall measurement of actuator performance could be obtained in terms of actuator displacement and torque output over multiple frequencies.

This overall actuator performance is plotted in Figure 46. As observed in the figure and as expected, the actuator has the highest output torque and highest displacement at quasi-static operation. As frequencies are increased, the maximum torque and displacement are diminished. Importantly, at 5 Hz, or near typical 1/Rev for most helicopters, the actuator is capable of outputting  $\pm 14^\circ$  and nearly 400 in-lbs, which likely would be sufficient for swashplateless actuation. If more torque output would be required, then many actuator variables could be adjusted to obtain the required performance level, such as actuator

length, dividing arm length, etc., without adding deleterious weight. In addition to high torque and displacement output at 1/Rev, the current actuator also can also provide significant output at 2/Rev, or roughly 10 Hz. As observed in Figure 46, the maximum output at 10 Hz is nearly 200 inlb and  $\pm 10^{\circ}$ .

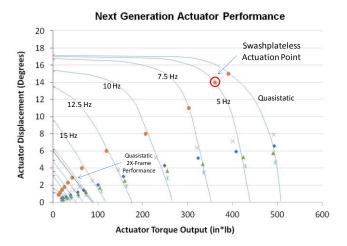


Figure 46. Next generation actuator performance over varying frequencies and applied torque levels.

## Current TRL: TRL 4

#### **Publications and Patent Applications**

#### Patent:

US Patent Title: "Pneumatic Actuator System for a Rotating Blade" Inventor: Dr. Joseph Szefi, Invercon, LLC

Filing Date: February 3<sup>rd</sup>, 2011

## References

- [1] Coffman, H.J., "Helicopter Rotor Icing Protection Methods," Journal of the American Helicopter Society, Vol. 32, No. 2, April 1987, pp. 34 39.
- [2] Szefi, J. T., Cormier, B., and Ionno, L., "Full-scale Experimental Validation of Dynamic, Centrifugally Powered, Pneumatic Actuators for Active Rotor Blade Surfaces," 70<sup>th</sup> American Helicopter Society Annual Forum and Technology Display, Montreal, Quebec, May 20-22, 2014. (D1876-08).

- [3] Ali, A., Hosseini, M., and Sahari, B., B., "A Review of Constitutive Models for Rubber –Like Materials", American Journal of Engineering and Applied Sciences, Vol. 3, No. 1, March 2010, pp. 232-239.
- [4] MSC Software White Paper, "Nonlinear Finite Element Analysis of Elastomers", Santa Ana, CA., 2010.
- [5] Cheremisinoff, N., P., Boyko, R., and Leidy, L., *Elastomer Technology Handbook*, CRC Press Inc., Boca Raton, FL., 1993, pp. 580.
- [6] Palacios, J., Wolfe, D., Bailey, M., Szefi, J., "Ice Testing of a Centrifugally Powered Pneumatic Deicing System for Helicopter Rotor Blades," 70<sup>th</sup> American Helicopter Society Annual Forum and Technology Display, Montreal, Quebec, May 20-22, 2014.
- [7] Turon, A., Camanho, P.P., Costa, J., Davila, C.G., "A Damage Model for the Simulation of Delamination of Advanced Composites under Variable-Mode Loading," Mechanics of Materials, Vol. 38, August, 2005.
- [8] Federal Aviation Regulation Part 25 "Airworthiness Standards: Transport Category Airplanes" and Part 29 "Airworthiness Standards: Transport Category Rotorcraft", FAA, Washington DC.
- [9] Yeo, H., and Chopra, I., "CFD-CSD Analysis of Active Control of Helicopter for Performance Improvement," American Helicopter Society 65th Annual Forum Proceedings, Grapevine, TX, May 27-29, 2009.
- [10] Shen., J., and Chopra, I., "Swashplateless Helicopter Rotor System with Trailing- Edge Flaps for Flight and Vibration Controls," Journal of Aircraft, Vol 43, No. 2, Apr-May 2006, pp. 346-352.
- [11] Bluman, James, E., "Reducing Trailing Edge Flap Deflection Requirements in Primary Control through a Moveable Horizontal Tail," Aerospace Engineering, PSU Master's Thesis, 2008.
- [12] Chopra, I., Shen, J., "Actuation Requirements of Swashplateless Trailing-Edge Flap Helicopter Rotor in Maneuvering and Autorotation Flights" AHS 60th Annual Forum, Baltimore, Maryland, June 7-10, 2004.
- [13] Duling, C. Gandhi, F., Straub, F., "On Power and Actuation Requirement in Swashplateless Primary Control using Trailing-Edge Flaps", AHS 66th Annual Forum, Phoenix, Arizona, May 11-13, 2010.
- [14] Shen, J., Chopra, I., Johnson, W., "Performance of Swashplateless Ultralight Helicopter Rotor with Trailing-Edge Flaps for Primary Flight Control," AHS Forum 59, Phoenix, AZ, 2003.